J. Am. Chem. Soc. **2000,** *122,* 8511−8523 8511

Excited-State Exchange Coupling in Bent Mn(III)−O−Mn(III) Complexes: Dominance of the π/σ Superexchange Pathway and Its Possible Contributions to the Reactivities of Binuclear Metalloproteins

Thomas C. Brunold,[†] Daniel R. Gamelin,[‡] and Edward I. Solomon*

Contribution from the Department of Chemistry, Stanford University, Stanford, California 94305

Received January 24, 2000. Revised Manuscript Received May 22, 2000

Abstract: Spectroscopic and computational studies of the mono-oxo-bridged complex $[\mathrm{Mn(III)_2O(OAc)_2(Me_3tacn)_2}]^{2+}$ (μ-O,Me$_3$tacn, where Me$_3$tacn denotes 1,4,7-trimethyl-1,4,7-triazacyclononane) are presented and discussed. The polarized single-crystal absorption spectra exhibit marked changes with increasing temperature between 10 and 300 K, in particular a significant red-shift and a broadening of the dominant feature in the visible spectral region. These data serve as the basis for evaluating density functional theory calculations to obtain quantitative molecular orbital descriptions of the dominant Mn−O−Mn superexchange pathways in μ-O,Me$_3$tacn. Both the spectroscopic and computational data indicate that the mixed π/σ Mn(xz)−O−Mn(z^2) superexchange pathway (where x and z are in the Mn−O−Mn plane and z is oriented along the Mn−O vector) produces the key contribution to exchange coupling. The weak ferromagnetic coupling in the ground state ($J = +9$ cm^{-1}, $H = -2J\mathbf{S_1S_2}$) results from a near cancellation of ferromagnetic and antiferromagnetic contributions. Upon d → d excitation ferromagnetic pathways are converted into antiferromagnetic pathways, leading to sizable antiferromagnetic exchange interactions in the ligand-field excited states. This gives rise to the observed red-shifts of the corresponding absorption bands with increasing temperature (i.e., population of thermally accessible ground-state spin sublevels with $S < 4$). To obtain deeper insight into the origin of the ferromagnetic ground-state coupling a valence-bond configuration interaction model is modified to include metal-to-metal charge-transfer excited states involving the unoccupied Mn d orbitals. It is shown that the contribution to J from a superexchange pathway can be used to estimate the value of the corresponding electronic coupling matrix element H_{AB} for electron transfer. Possible implications of our results for the binuclear metalloproteins manganese catalase, hemerythrin, and ribonucleotide reductase are discussed.

Introduction

Binuclear mono-oxo-bridged Mn(III)$_2$ and Fe(III)$_2$ complexes have been under intense study because of their relevance to metalloprotein active sites.[1−4] A striking feature of these complexes is that the ground-state magnetic exchange coupling constant J exhibits a strong dependence on the identity of the metal ions and on the bridging angle.[5−7] While the Mn(III) centers in $[\mathrm{Mn(III)_2O(OAc)_2\ (Me_3tacn)_2}]^{2+}$ (r(Mn−O) = 1.81 Å, ∠(Mn−O−Mn) = 121°,[8] see Chart 1) are weakly ferromagnetically exchange coupled,[9] $J = +9$ cm^{-1} ($H = -2J\mathbf{S_1S_2}$), the Fe(III) centers in the iron analogue (r(Fe−O) = 1.79 Å, ∠(Fe−O−Fe) = 120°) exhibit strong antiferromagnetic coupling,[10] $J = -119$ cm^{-1}. Further, the nature of the magnetic exchange interaction in oxo-bridged Mn(III)$_2$ dimers changes from essentially uncoupled in bent complexes[2,9,11] to strongly antiferromagnetic,[12] $J = -120$ cm^{-1}, in a nearly linear dimer (r(Mn−O) = 1.76 Å, ∠(Mn−O−Mn) = 168°), whereas oxo-bridged Fe(III)$_2$ dimers generally exhibit strong antiferromagnetic exchange coupling with a minor dependence on the Fe−O−Fe angle.[4,13,14]

Chart 1. Core Atoms of μ-O,Me$_3$tacn and Coordinate Frames

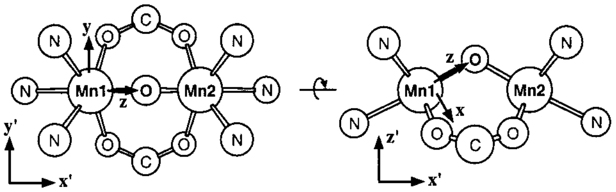

[†] Present address: Department of Chemistry, University of Wisconsin, Madison, WI 53706.

[‡] Present address: Department of Chemistry, University of Washington, Seattle, WA 98195.

(1) Holm, R. H.; Kennepohl, P.; Solomon, E. I. *Chem. Rev.* **1996**, *96*, 2239.

(2) Wieghardt, K. *Angew. Chem., Int. Ed. Engl.* **1989**, *28*, 1153.

(3) Yachandra, V. K.; Sauer, K.; Klein, M. P. *Chem. Rev.* **1996**, *96*, 2927.

(4) Kurtz, D. M., Jr. *Chem. Rev.* **1990**, *90*, 585.

(5) Bossek, U.; Weyermüller, T.; Wieghardt, K.; Bonvoisin, J.; Girerd, J.-J. *J. Chem. Soc., Chem. Commun.* **1989**, 633.

(6) Hotzelmann, R.; Wieghardt, K.; Flörke, U.; Haupt, H.-J.; Weatherburn, D. C.; Bonvoisin, J.; Blondin, G.; Girerd, J.-J. *J. Am. Chem. Soc.* **1992**, *114*, 1681.

(7) Weihe, H.; Güdel, H. U. *J. Am. Chem. Soc.* **1998**, *120*, 2870.

(8) Wieghardt, K.; Bossek, U.; Ventur, D.; Weiss, J. *J. Chem. Soc., Chem. Commun.* **1985**, 347.

(9) Wieghardt, K.; Bossek, U.; Nuber, B.; Weiss, J.; Bonvoisin, J.; Corbella, M.; Vitols, S. E.; Girerd, J.-J. *J. Am. Chem. Soc.* **1988**, *110*, 7398.

(10) Hartmann, J. A.; Rardin, R. L.; Chaudhuri, P.; Pohl, K.; Wieghardt, K.; Nuber, B.; Weiss, J.; Papaefthymiou, G. C.; Frankel, R. B.; Lippard, S. J. *J. Am. Chem. Soc.* **1987**, *109*, 7387.

(11) Ménage, S.; Girerd, J.-J.; Gleizes, A. *J. Chem. Soc., Chem. Commun.* **1988**, 431.

(12) Kipke, C. A.; Scott, M. J.; Gohdes, J. W.; Armstrong, W. H. *Inorg. Chem.* **1990**, *29*, 2193.

(13) Gorun, S. M.; Lippard, S. J. *Inorg. Chem.* **1991**, *30*, 1625.

(14) Weihe, H.; Güdel, H. U. *J. Am. Chem. Soc.* **1997**, *119*, 6539.

10.1021/ja000264l CCC: $19.00

Significant research effort has been undertaken to obtain insight into the magnetic properties of bent oxo-bridged dimers. An elegant approach was employed by Wieghardt, Girerd, and co-workers who prepared the heterobinuclear complex [Mn(III)/Fe(III)O(OAc)$_2$(Me$_3$tacn)$_2$]$^{2+}$.[5,6] The fairly strong antiferromagnetic exchange coupling, $J = -73$ cm^{-1}, permitted them to conclude that the in-plane, mixed π/σ Mn(xz)$-$O$-$Fe(z^2) superexchange pathway[15] (where the local **z** axis on each metal is oriented along the metal$-$O bond vector, see Chart 1) produces the dominant contribution to J rather than the symmetric σ/σ Mn(z^2)$-$O$-$Fe(z^2) pathway because the Mn z^2 orbital is unoccupied in that dimer. A complication of their analysis arises from the fact that it is based on a heterobinuclear complex. Due to differences in the effective nuclear charges of Mn(III) and Fe(III) the d-orbital manifolds of the two metal ions are energetically displaced from each other, and the dominance of the mixed pathway could thus arise from a near degeneracy of the half-occupied Mn(III) xz and Fe(III) z^2 orbitals, which would permit extensive mixing between these two orbitals.

Using an angular overlap model, Weihe and Güdel analyzed the magnetic properties of the series of trivalent homobinuclear and heterobinuclear oxo-bridged complexes ranging from Ti(III)$_2$ (d^1d^1) through Fe(III)$_2$ (d^5d^5).[7] Consistent with Wieghardt and Girerd's results,[5,6] the mixed π/σ M(xz)$-$O$-$M(z^2) superexchange pathway was found to be dominant in the bent dimers. Although an excellent correspondence between experimental and calculated ground-state exchange coupling constants was achieved, the model employed was based upon the assumption that the parameters are transferable between all dimers and again did not take into account the large variation in effective nuclear charges of the metal ions across the series of complexes.

Recently we employed density functional theory (DFT) calculations to investigate the molecular mechanism of dioxygen binding to hemerythrin (Hr), a binuclear non-heme iron protein that functions as an O$_2$ carrier in certain invertebrates.[16,17] In the oxygenation reaction of Hr, one electron from each Fe(II) center and the proton from the bridging hydroxide of the diferrous site are transferred to O$_2$ that binds to a single iron center, yielding an oxo-bridged diferric site possessing a terminal hydroperoxide.[18] A key result from our studies is that the electron transfer (ET) from the noncoordinated iron to O$_2$ is coupled to the proton transfer, and that this ET also involves the mixed π/σ Fe(xz)$-$O$-$Fe(z^2) superexchange pathway. In our model, this pathway serves both the roles of affording a large electronic coupling matrix element for rapid ET between the two metal centers and of producing a significant contribution to the driving force of O$_2$ binding to Hr by stabilizing the singlet ground state of the antiferromagnetically coupled oxyHr site. Given the fact that the mixed π/σ pathway appears to be key to the proper functioning of Hr and other bent oxo-bridged binuclear metalloprotein active sites, a direct experimental probe of the relative importance of this superexchange pathway in oxo-bridged dimers is of great interest.

In the past we successfully employed an excited-state spectroscopic approach for a direct analysis of individual superexchange pathways in Cu(II)$_2$ acetate.[19] From the observed dimer splittings in the LF excited states detailed information about the exchange interactions between different combinations of half-occupied Cu d orbitals on adjacent metal centers could be extracted, which provided significant insight into the orbital origin of the spin Hamiltonian parameters in copper dimers. Using a similar spectroscopic approach for the study of [Fe(III)$_2$O(OAc)$_2$(Me$_3$tacn)$_2$]$^{2+}$, we observed that elimination of the mixed π/σ Fe$-$O$-$Fe pathway in a ligand-field (LF) excited state gives rise to ferromagnetic coupling;[20] however, quantitative analysis of these data was complicated by the spin-forbidden nature of the corresponding LF transition and the large antiferromagnetic exchange coupling in the ground state.

In the present study variable-temperature polarized single-crystal absorption spectroscopy is employed to experimentally probe the efficiency of individual superexchange pathways in the homobinuclear bent oxo-bridged model dimer [Mn(III)$_2$O(OAc)$_2$(Me$_3$tacn)$_2$]$^{2+}$. We take advantage of the fact that Mn(III) complexes, unlike their Fe(III) analogues, exhibit four spin-allowed ligand-field (LF) transitions that involve excitation of an electron from one of the four-half-occupied d orbitals to the single unoccupied d orbital (corresponding to the z^2 orbital, which is part of the mixed superexchange pathway that is therefore “switched on” in the LF excited states), permitting a direct correlation between absorption band maxima and d orbital splittings. Further, the nature of the magnetic exchange interaction in [Mn(III)$_2$O(OAc)$_2$(Me$_3$tacn)$_2$]$^{2+}$ is weakly ferromagnetic,[9] $J = +9$ cm^{-1}, and the entire spin manifold of the exchange-split dimer ground state is thermally accessible. From the temperature dependence of the absorption spectrum we obtain signs and magnitudes of the exchange coupling constants in the LF excited states. These data are complemented by DFT calculations and analyzed within the framework of a valence-bond configuration interaction (VBCI) model[21] to obtain insight into the orbital origin of magnetic exchange interactions in oxo-bridged Mn(III)$_2$ dimers. The VBCI model is further employed to relate the contribution to J from a superexchange pathway to the magnitude of the electronic coupling matrix element for intramolecular metal$-$metal ET in the homovalent dimer and its one-electron reduced mixed valence analogue. The significance of our results with respect to the binuclear metalloprotein active sites of manganese catalase, hemerythrin, and ribonucleotide reductase is discussed.

2. Experimental Section

Samples of [Mn(III)$_2$O(OAc)$_2$(Me$_3$tacn)$_2$](ClO$_4$)$_2$·H$_2$O (referred to as μ-O,Me$_3$tacn below) and [Mn(III)$_2$O(OAc)$_2$(H$_2$O)$_2$(bipy)$_2$](PF$_6$)$_2$·(H$_2$O)$_{1.75}$ were prepared as described in the literature.[8,11] Solid-state data on polycrystalline samples were obtained in poly(dimethylsiloxane) mulling agent. Single crystals of μ-O,Me$_3$tacn suitable for optical absorption measurements were grown directly on the quartz disks used in the sample mount by slowly evaporating the acetonitrile solvent at 4 °C. μ-O,Me$_3$tacn crystallizes in the orthorhombic space group *Amam* with four symmetry-related molecules per unit cell.[8] The dimeric unit possesses crystallographically imposed C_{2v} symmetry with all Mn···Mn vectors aligned parallel to **c**, and each monomer half has C_s symmetry with a mirror plane perpendicular to **a**. Crystals of μ-O,Me$_3$tacn exhibit a marked dichroism; they are deep red in color for linearly polarized light with $\mathbf{E} \perp \mathbf{a}$ (in-plane polarized) and colorless for $\mathbf{E} \parallel \mathbf{a}$ (out-of-plane polarized).

Variable-temperature absorption spectra were measured on a double-beam spectrophotometer (Cary 17) using a liquid helium cryostat (Janis Research Super Vari-Temp). A pair of Glan-Taylor polarizers matched from 200 nm to 2.5 μm were used for single-crystal experiments. MCD data were collected on CD spectropolarimeters (Jasco J200 and J500)

---

[15] An abbreviated notation is used to designate d orbitals; e.g., z^2 stands for d_{z^2}.

[16] Brunold, T. C.; Solomon, E. I. *J. Am. Chem. Soc.* **1999**, *121*, 8277.

[17] Brunold, T. C.; Solomon, E. I. *J. Am. Chem. Soc.* **1999**, *121*, 8288.

[18] Stenkamp, R. E. *Chem. Rev.* **1994**, *94*, 715.

[19] Ross, P. K.; Allendorf, M. D.; Solomon, E. I. *J. Am. Chem. Soc.* **1989**, *111*, 4009.

[20] Brown, C. A.; Remar, G. J.; Musselman, R. L.; Solomon, E. I. *Inorg. Chem.* **1995**, *34*, 688.

[21] Tuczek, F.; Solomon, E. I. *Inorg. Chem.* **1993**, *32*, 2850.

with sample compartments modified to accommodate magnetocryostats (Oxford Instruments). A resonance Raman excitation profile for solid μ-O,Me$_3$tacn was recorded upon excitation with Kr$^+$ (Coherent Innova 90C-K) and Ar$^+$ (Coherent Sabre 25/7) ion lasers with incident power in the 5−25 mW range using an ~135° backscattering arrangement. The scattered light was dispersed by a triple monochromator (Spex 1877 CP, equipped with 1200, 1800, and 2400 grooves/mm gratings) and analyzed with a back-illuminated CCD camera (Princeton Instruments ST-135). Raman intensities were quantitated relative to the 984 cm^{-1} scattering peak of K$_2$SO$_4$.

Electronic structure calculations on an approximate μ-O,Me$_3$tacn model (with formates replacing acetates and NH$_3$ groups modeling the Me$_3$tacn ligation) were performed on an IBM 3BT-RS/6000 computer using the Amsterdam Density Functional (ADF) program version 2.0.1 developed by Baerends et al.[22] The model used, along with the molecular (primed) and local (unprimed) coordinate frames, is shown in Chart 1, and atomic coordinates are listed in Table S1 (Supporting Information). A triple-ζ Slater-type orbital basis set with a single polarization function (ADF basis set IV) was used for each atom. Core orbitals were frozen through 1s (C, N, O) and 3p (Mn). Calculations were performed single point using the local density approximation of Vosko, Wilk, and Nusair[23] for the exchange and correlation energy and the nonlocal gradient corrections of Becke[24] and Perdew.[25] An accuracy parameter of 4.0 was chosen for the numerical integration grid. Graphical output of the computational results was generated with the Cerius^2 software program developed by Molecular Simulations Inc.

3. Results and Analysis

Spectroscopy. Solid-state low-temperature electronic absorption, MCD, and resonance Raman excitation profile data of μ-O,Me$_3$tacn are shown in Figure 1.[26] The 5 K absorption spectrum (Figure 1, top) consists of a broad band *I* centered at ~13700 cm^{-1} ($\epsilon \approx 250$ M^{-1} cm^{-1}) and a more intense broad feature *II* extending from about 17000 to 22500 cm^{-1} ($\epsilon \approx 900$ M^{-1} cm^{-1}).[27] At higher energy, the onset to a strong UV absorption band with a maximum above 30000 cm^{-1} is observed. The resonance Raman excitation profile for the symmetric Mn−O−Mn stretching mode, ν(Mn−O) ≈ 552 cm^{-1}, shows practically no enhancement below 22000 cm^{-1}, but strongly increases in intensity into the UV region (● in Figure 1, top), indicating that bands *I* and *II* correspond to ligand field (LF) transitions of Mn(III). In the 4.5 K MCD spectrum (Figure 1, bottom) some sharper features are observed in the 17000−22000 cm^{-1} range in addition to the broad bands arising from spin-allowed LF transitions of Mn(III). These features coincide with the fine structure in the region of band *II* in absorption (Figure 1, top) and are assigned to spin-forbidden spin-flip transitions of Mn(III).[28]

The temperature dependence of the solid-state mull absorption spectrum of μ-O,Me$_3$tacn in the visible region is shown in the inset of Figure 1. With increasing temperature band *II* exhibits a dramatic change in shape, consisting of a gradual decrease in the high-energy region in parallel with an increase on its low-energy side. This behavior can be qualitatively understood in terms of a gradual population of thermally accessible spin sublevels of the weakly ferromagnetically coupled ground state of μ-O,Me$_3$tacn, $J = +9$ cm^{-1} ($H = -2J\mathbf{S_1S_2}$).[9] To test this model variable-temperature absorption data were taken on the weakly antiferromagnetically coupled dimer [Mn(III)$_2$O(OAc)$_2$(H$_2$O)$_2$(bipy)$_2$](PF$_6$)$_2$•(H$_2$O)$_{1.75}$, $J = -3.4$ cm^{-1}.[11] As expected from the reversed ground-state spin sublevel splitting, the temperature dependence of the corresponding absorption spectrum is opposite to that observed for μ-O,Me$_3$tacn; that is, with increasing temperature band *II* shows an increase in intensity on its high-energy side (Figure S1, Supporting Information).[29]

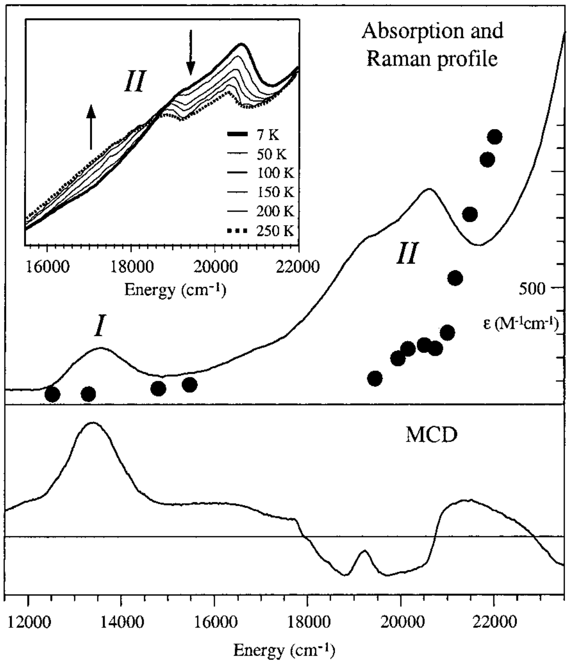

Figure 1. Solid-state mull absorption (5 K) and MCD (4.5 K, 5.5 T) spectra of μ-O,Me$_3$tacn (modified from ref 26). The ~120 K resonance Raman excitation profile for the symmetric Mn−O stretching mode (●) is superimposed on the absorption spectrum. Inset: Temperature dependence (5 K → 300 K) of the absorption spectrum in the region of band *II*.

To further explore the temperature dependence of the electronic absorption spectrum of μ-O,Me$_3$tacn and to eliminate light scattering effects that are inherent in mull absorption data, the **E** ∥ **a** and **E** ⊥ **a** polarized single crystal spectra were measured in the visible and near-IR regions (Figure 2, top). The two polarizations are strikingly different: while band *I* is **E** ∥ **a** polarized (perpendicular to the Mn−O−Mn plane), band *II* is present only in **E** ⊥ **a** polarization. Both features exhibit remarkable, yet very distinct temperature dependencies. Between 10 and 300 K band *I* changes only slightly in shape, but decreases by about 40% in intensity. In the same temperature range, band *II* shows a significant intensity redistribution from higher to lower energy, whereas the integrated absorption intensity remains approximately constant.

Dimer Selection Rules. The main features in the absorption spectrum of μ-O,Me$_3$tacn (Figure 1) were previously assigned on the basis of 10 K polarized single-crystal absorption data and DFT calculations for the ferromagnetic ($S = 4$) dimer ground state.[26] In the following these results are used as a starting point for the analysis of the dramatic temperature effects observed for bands *I* and *II* (Figure 2).

---

[22] (a) Baerends, E. J.; Ellis, D. E.; Ros, P. *Chem. Phys.* **1973**, *2*, 42. (b) te Velde, G.; Baerends, E. J. *Int. J. Comput. Phys.* **1992**, *99*, 84.

[23] Vosko, S. H.; Wilk, L.; Nusair, M. *Can. J. Phys.* **1980**, *58*, 1200.

[24] Becke, A. D. *J. Chem. Phys.* **1986**, *84*, 4524.

[25] Perdew, J. P. *Phys. Rev. B* **1986**, *33*, 8822.

[26] Brunold, T. C.; Gamelin, D. R.; Stemmler, T. L.; Mandal, S. K.; Armstrong, W. H.; Penner-Hahn, J. E.; Solomon, E. I. *J. Am. Chem. Soc.* **1998**, *120*, 8724.

[27] Note that bands *I* and *II* in Figure 2 were designated bands *II* and *III*, respectively, in ref 26.

[28] Pelletier, Y.; Reber, C. *Can. J. Chem.* **1995**, *73*, 249.

[29] The temperature effect is weak, however, partly because the dimeric unit in that complex possesses only C_I symmetry.[11] This results in a larger number of allowed transitions and, therefore, in significant overlap of absorption features in the region of band *II*. In addition, temperature effects in the mull spectra are attenuated due to light scattering effects (cf. Figures 1 (inset) and 2).

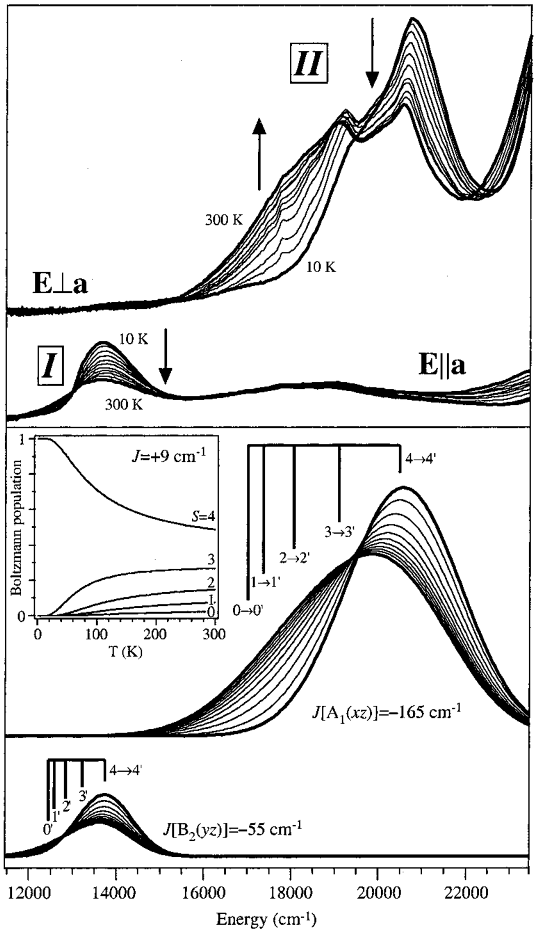

Figure 2. Top: **E** || **a** and **E** ⊥ **a** polarized single-crystal absorption spectra of μ-O,Me$_3$tacn between 10 and 300 K. Note that the sharp features in **E** ⊥ **a** polarization are due to spin-forbidden spin-flip transitions of Mn(III). Bottom: Simulation of the variable temperature behavior of the experimental spectra (see text for details). The positions of the spin allowed transitions from the individual spin sublevels of the exchange coupled dimer ground state are indicated on top of the simulated curves. Inset: Boltzmann populations as a function of temperature of the ground-state spin sublevels, obtained with $J = +9$ cm^{-1}.

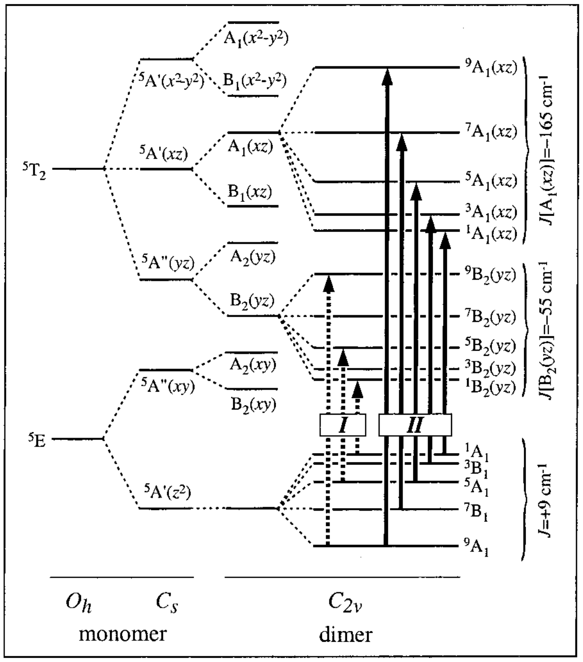

Figure 3. Schematic energy level diagram for the quintet ligand field (LF) states of Mn(III) in μ-O,Me$_3$tacn illustrating the effects of the $O_h \rightarrow C_s$ symmetry reduction and dimer formation. The electric dipole allowed transitions in the C_{2v} dimer symmetry corresponding to bands *I* and *II* are indicated by arrows: dotted lines for **E** || **y(a)** and solid lines for **E** ⊥ **y(a)**.

A schematic energy level diagram of the ligand field (LF) states of Mn(III) (3d^4 electron configuration) in μ-O,Me$_3$tacn is shown in Figure 3. The dominant LF component associated with the bridging oxide lifts the degeneracies of the five d orbitals of Mn(III) and leaves the z^2 orbital[15] that is oriented toward this bridge unoccupied. In the dimer ground-state ferromagnetic exchange coupling[9] ($J = +9$ cm^{-1}) between the two $S = 2$ monomers gives rise to the spin ladder shown in the right bottom half of Figure 3. The LF excited states in the dimer are obtained by coupling the $^5A'(z^2)$ ground state of one Mn(III) center with the quintet excited states of its partner[30] (a hole notation is used to designate the C_s monomer and C_{2v} dimer exited states). Since either one of the two metal ions can be excited, the proper dimer wave functions are obtained from symmetric and antisymmetric combinations of the locally excited configurations. The corresponding states are split in energy due to Coulomb and exchange-mediated excitation transfer between the Mn(III) centers[19,31,32] (Figure 3, center). Further, each excited state is split into $2S + 1 = 1, 3, ..., 9$ spin components by magnetic exchange interactions between the two Mn(III) centers. Band assignments in the absorption spectrum of μ-O,Me$_3$tacn are facilitated by the rigorous C_{2v} symmetry of the dimeric unit and by the ferromagnetic exchange coupling between the Mn(III) centers in the ground state[9] ($J = +9$ cm^{-1}); that is, the only transitions contributing to the low-temperature absorption spectrum originate from the $^9A_1$ level. On the basis of the selection rules and DFT calculations for the high spin ($S = 4$) ground state, bands *I* and *II* in the polarized 10 K absorption spectra of μ-O,Me$_3$tacn (Figure 2) were assigned to the $^9A_1 \rightarrow {}^9B_2(yz)$ (**E** || **y′**(**a**) polarized, see Chart 1 for axes orientations) and $^9A_1 \rightarrow {}^9A_1(xz)$ (**E** ⊥ **y′**(**a**) polarized) transitions, respectively, indicated by arrows in Figure 3 (right).[26]

The absorption intensity of band *II* is substantially higher than typically observed for d → d bands of six-coordinate Mn(III) complexes.[33] This was ascribed to the large oxo *p* orbital character in the Mn *xz*-based donor and z^2-based acceptor orbitals involved in the $^9A_1 \rightarrow {}^9A_1(xz)$ transition.[26] The low energy of band *I* relative to band *II* (Figure 1) is due to a very strong out-of-plane π-antibonding interaction between the bridging oxide and the manganese centers, which leads to a large destabilization of the Mn *yz*-based molecular orbital and consequently to a small energy splitting between the donor and acceptor orbitals for $^9A_1 \rightarrow {}^9B_2(yz)$ excitation. While five-coordinate Mn(III) complexes in general exhibit similarly high absorption intensity in the region of band *II*,[34,35] band *I* is unique to oxo-bridged Mn(III)$_2$ dimers and thus provides a spectral probe for the presence of a bridging oxide in manganese(III) dimers.

---

[30] Hirst, L. L.; Ray, T. *Proc. R. Soc. London, A* **1982**, *384*, 191.

[31] Eickman, N. C.; Himmelwright, R. S.; Solomon, E. I. *Proc. Natl. Acad. Sci. U.S.A.* **1979**, *76*, 2094.

[32] Güdel, H. U.; Weihe, H. In *Molecular Magnetism: From Molecular Assemblies to the Devices;* Coronado, E. et al., Eds.; Kluwer Academic: Netherlands, 1996; pp 173−197.

[33] Lever, A. B. P. *Inorganic Electronic Spectroscopy*, 2nd ed.; Elsevier Science Publishers B. V.: Amsterdam, 1984.

[34] (a) Dingle, R. *Inorg. Chem.* **1965**, *4*, 1287. (b) Dingle, R. *Acta Chem. Scand.* **1966**, *20*, 33. (c) Dingle, R. *J. Mol. Spectrosc.* **1962**, *9*, 426.

An important property of exchange-coupled dimer ground states relates to the fact that the orbital parts of the spin sublevel wavefunctions can exhibit distinct transformation behavior.[30] As shown in Figure 3 (right bottom) in μ-O,Me$_3$tacn the spin sublevels transform as A_1 for $2S + 1 = 9$, 5, and 1, and as B_1 for $2S + 1 = 7$ and 3. In contrast, all spin components of a given LF excited state have the same symmetry, as indicated for the $^{2S+1}B_2(yz)$ and $^{2S+1}A_1(xz)$ excited states (Figure 3, right). This leads to the interesting situation that only transitions from the $^9A_1$, $^5A_1$, and $^1A_1$ components of the ground state are electric-dipole allowed to the $^{2S+1}B_2(yz)$ excited state (band *I*), in $\mathbf{E} \parallel \mathbf{y}'(\mathbf{a})$ polarization, whereas transitions originating from all ground-state spin sublevels are allowed to $^{2S+1}A_1(xz)$ (band *II*), with $\mathbf{E} \perp \mathbf{y}(\mathbf{a})$. (Note that the polarization of the latter transition alternates between $\mathbf{E} \parallel \mathbf{z}'(\mathbf{b})$ and $\mathbf{E} \parallel \mathbf{x}'(\mathbf{c})$ as a function of *S*; we do not experimentally resolve these polarizations in the $\mathbf{E} \perp \mathbf{y}(\mathbf{a})$ spectrum). Thus, the decrease in absorption intensity of band *I* with increasing temperature can be explained in terms of thermal population of the $^7B_1$ and $^3B_1$ components of the exchange-split ground state from which transitions to $^7B_2(yz)$ and $^3B_2(yz)$, respectively, are forbidden in the dimer symmetry (Figure 3, right).

The presence of thermally accessible ground-state spin sublevels with $S < 4$ is also responsible for the unusual chromatic shift of band *II* in the variable temperature absorption spectra of μ-O,Me$_3$tacn (Figure 2). As indicated in Figure 3, a red-shift of an absorption band with increasing temperature will occur if the corresponding excited state is subject to antiferromagnetic energy splittings. Thus, the marked red-shift of band *II* between 10 and 300 K is a direct experimental manifestation of strong antiferromagnetic exchange interactions between the two Mn(III) centers in the $^{2S+1}A_1(xz)$ excited state. To estimate the magnitude of the corresponding exchange coupling constant, $J[A_1(xz)]$, the spin sublevel splitting in the excited state was modeled by a Landé pattern, and the absorption spectrum was simulated in terms of a sum of five Gaussians of fixed width, one band for each spin component of $^{2S+1}A_1(xz)$, with intensities that were scaled according to the Boltzmann population in the ground state (inset in Figure 2, bottom). Despite the simplicity of this model, the essential features of the experimental spectra (Figure 2, top) are reasonably well reproduced by the simulation for $J[A_1(xz)] = -165$ cm^{-1} (Figure 2, bottom). A similar approach was used to estimate $J[B_2(yz)]$ from the variable temperature behavior of band *I*, except that the intensities of the Gaussians corresponding to the triplet and septet components were scaled to zero since transitions from the $^3B_1$ and $^7B_1$ ground-state levels are forbidden in the dimer symmetry (Figure 3, right). The simulated spectra obtained with $J[B_2(yz)] = -55$ cm^{-1} are shown in Figure 2, bottom. The observed decrease in total intensity of band *I* with increasing temperature (Figure 2, top) is well reproduced.

In summary, the strong variation of the polarized absorption intensity of μ-O,Me$_3$tacn with temperature (Figure 2, top) arises from a thermal population of spin sublevels with $S < 4$ of the ferromagnetically coupled dimer ground state (Figure 3, right). Quantitative analysis of the temperature dependencies of bands *I* and *II* leads to estimates for the exchange coupling constants of $J[B_2(yz)] = -55$ cm^{-1} and $J[A_1(xz)] = -165$ cm^{-1}, respectively. Thus, upon $yz \rightarrow z^2$ and $xz \rightarrow z^2$ electronic excitations the nature of the exchange interaction in μ-O,Me$_3$tacn changes from weakly ferromagnetic in the ground state to antiferromagnetic in the corresponding LF excited states. Because both transitions involve promotion of an electron to the same Mn z^2-based acceptor orbital, the stronger coupling in the $^{2S+1}A_1(xz)$ state than in the $^{2S+1}B_2(yz)$ state indicates that *J* is sensitive to the orientation of the unoccupied orbital in the excited state associated with these transitions.

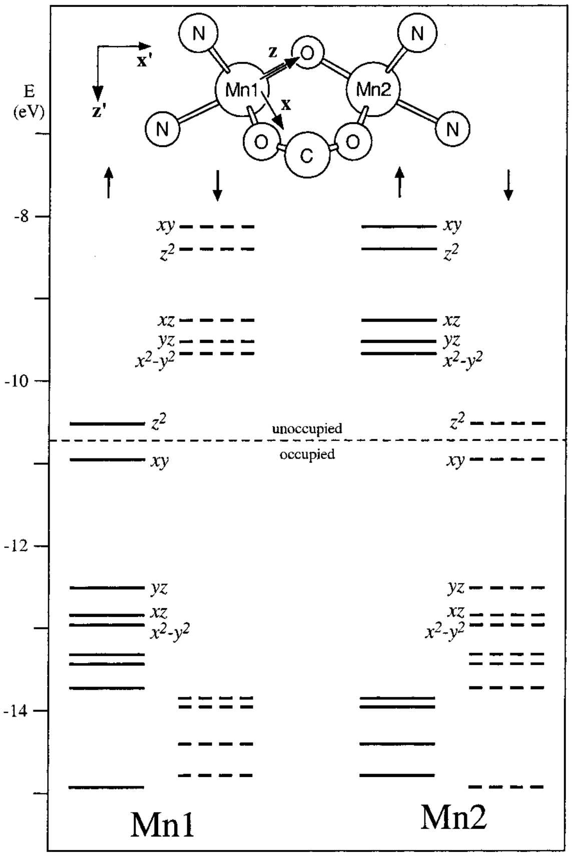

Figure 4. Energy level diagram obtained from a spin-unrestricted BS ($M_S = 0$) DFT calculation on μ-O,Me$_3$tacn. Spin-up and spin-down levels are shown by solid and broken lines, respectively. Top portion: Computational model employed, along with the molecular (primed) and local (unprimed) coordinate frames.

MO Description of Superexchange Pathways. In this section the experimental data presented above are complemented by DFT calculations on the broken symmetry (BS) ground state of μ-O,Me$_3$tacn to obtain a quantitative description of the dominant superexchange pathways in this dimer. Similar calculations on the tacn analogue of μ-O,Me$_3$tacn and on other Mn dimers were previously reported by Noodleman and coworkers.[36] These studies focused on calculating charge and spin densities and ground-state exchange coupling constants, and the nature of individual superexchange pathways was not explored.

The relevant part of an energy level diagram obtained from a spin unrestricted BS ($M_S = 0$) DFT calculation on μ-O,Me$_3$tacn is shown in Figure 4, and the energies and compositions of the Mn1 d-based spin-up molecular orbitals (MOs) are given in Table 1. In the BS approach the dimer is treated as two weakly interacting antiferromagnetically coupled monomers, and the ground state is represented by a single determinant with the spin-up and spin-down electrons localized on Mn1 and Mn2, respectively.[37] Using the formalism developed by Noodleman[38]

---

(35) (a) Davis, T. S.; Fackler, J. P.; Weeks, M. J. *Inorg. Chem.* **1968**, *7*, 1994. (b) Boucher, L. J.; Herrington, D. R. *Inorg. Chem.* **1974**, *13*, 1105. (c) Boucher, L. J.; Day, V. W. *Inorg. Chem.* **1977**, *16*, 1360. (d) Wieghardt, K.; Pohl, K.; Bossek, U.; Nuber, B.; Weiss, J. *Z. Naturforsch.* **1988**, *43b*, 1184.

(36) Zhao, X. G.; Richardson, W. H.; Chen, J.-L.; Li, L.; Noodleman, L.; Tsai, H.-L.; Hendrickson, D. N. *Inorg. Chem.* **1997**, *36*, 1198.

(37) Noodleman, L.; Norman, J. G., Jr. *J. Chem. Phys.* **1979**, *70*, 4903.

Table 1. Energies (eV) and Compositions (%) of the Mn1 d-based Spin-up Molecular Orbitals Obtained from a BS DFT Calculation on μ-O,Me$_3$tacn[a]

		left	Mn1					μ-oxo			Mn2					right
level	energy	N,O′	x^2-y^2	xz	yz	xy	z^2	$p_{x'}$	$p_{y'}$	$p_{z'}$	x^2-y^2	xz	yz	xy	z^2	N,O′
							unoccupied									
z^2	−10.514	17	0	0	0	0	42	4	0	0	0	30	0	0	1	1
							occupied									
xy	−10.952	36	0	0	0	57	0	0	0	0	0	0	0	0	0	1
yz	−12.513	4	0	0	40	0	0	0	33	0	0	0	8	1	0	12
xz	−12.842	6	1	46	0	0	0	2	0	25	0	1	0	0	4	7
x^2-y^2	−12.960	18	65	1	0	0	0	0	0	0	1	0	0	0	0	11

[a] See Chart 1 for axes orientations. Entries for N,O′ give the sums of the total orbital contributions from N(NH$_3$) and O′(formate).

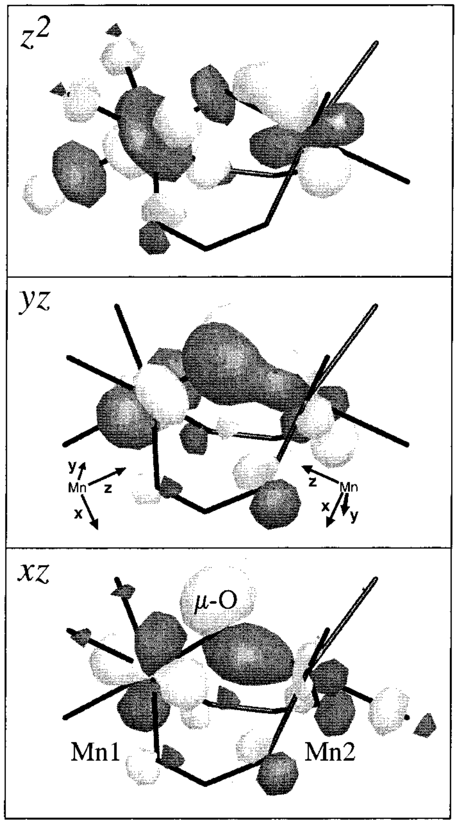

Figure 5. Boundary surface plots of the Mn1 d-based occupied *xz*, *yz*, and unoccupied z^2 spin up MOs obtained from a BS DFT calculation on μ-O,Me$_3$tacn.

to calculate the ground-state exchange coupling constant, a value of $J = -5$ cm^{-1} was obtained, in the range of experimental J values for bent oxo-bridged Mn(III)$_2$ dimers ($J = -4.1$ cm^{-1} antiferromagnetic to $+9$ cm^{-1} ferromagnetic[39]). Thus, our calculations are consistent with the small net exchange coupling in the ground state of bent Mn(III)−O−Mn(III) dimers, validating an analysis of the superexchange pathways on the basis of the calculated orbital descriptions.

Boundary surface plots of the Mn1 d-based spin-up orbitals involved in bonding interactions with the bridging oxide are shown in Figure 5. Both the Mn *xz* and *yz* orbitals exhibit strong π-antibonding interactions with the oxo $p_{z'}$ and $p_{y'}$ orbitals, respectively, leading to a large energy separation of the corresponding MOs from the Mn (x^2-y^2)-derived level (Figure 4) that is oriented perpendicular to the Mn1−oxo bond.[40] The Mn z^2 orbital participates in a strong σ-antibonding interaction with the bridging oxide (Figure 5, top), which results in a large destabilization of the unoccupied z^2-based MO relative to the occupied *xy*-derived orbital (Figure 4). This d-orbital splitting pattern reflects the dominant nature of the LF component associated with the bridging oxide, paralleling the results obtained from density functional calculations on the diiron(III) analogue.[20]

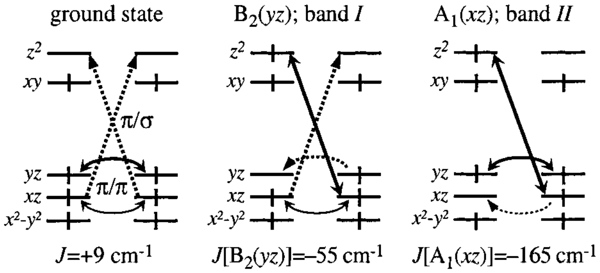

Figure 6. Schematic illustration of the dominant superexchange pathways in the ground state and the LF excited states corresponding to bands *I* and *II* of μ-O,Me$_3$tacn. Ferromagnetic and antiferromagnetic pathways are indicated by dotted and solid lines, respectively.

The effectiveness of the Mn1 d-based MOs for superexchange is governed by the extent of orbital contributions from the bridging oxide and the second manganese. Antiferromagnetic contributions to J arise from delocalization of the excess spin-up electron density localized on Mn1 onto Mn2-centered d orbitals whose spin-down counterparts are occupied. Thus, the major antiferromagnetic superexchange pathway in the ground state of μ-O,Me$_3$tacn involves the Mn1 *yz*-based MO (Figure 5, Table 1), corresponding to an out-of-plane symmetric π/π Mn1(*yz*)−O−Mn2(*yz*) pathway. A second, substantially smaller antiferromagnetic contribution to J originates from the in-plane π/π Mn1(*xz*)−O−Mn2(*xz*) pathway. Alternatively, the admixture of Mn2 z^2-orbital character to the Mn1 *xz*-based MO, corresponding to an in-plane mixed π/σ Mn1(*xz*)−O−Mn2(z^2) pathway, produces a ferromagnetic contribution to J because the Mn2 z^2-based spin-down MO is unoccupied.[41,42] The relevant ferromagnetic and antiferromagnetic superexchange pathways in the ground state of μ-O,Me$_3$tacn are indicated by arrows in the schematic energy level diagram shown in Figure 6 (left-hand side). The weak ground-state exchange coupling in μ-O,Me$_3$tacn indicates that the ferromagnetic, mixed π/σ (dotted arrows), and the antiferromagnetic, symmetric π/π (solid arrows), contributions to J are comparable in magnitude and sum to zero.

---

(38) Noodleman, L. *J. Chem. Phys.* **1981**, *74*, 5737.

(39) Corbella, M.; Costa, R.; Ribas, J.; Fries, P. H.; Latour, J.-M.; Öhrström, L.; Solans, X.; Rodriguez, V. *Inorg. Chem.* **1996**, *35*, 1857.

(40) Note that the **x** and **y** axes are rotated by 45° about **z** from their usual orientations along the metal−ligand bonds. Thus, the e_g set of Mn d orbitals comprises the z^2 and *xy* orbitals.

(41) Expressions in the early literature for kinetic exchange in exchange-coupled systems have recently been analyzed by second-order perturbation theory.[42]

(42) Weihe, H.; Güdel, H. U. *Inorg. Chem.* **1997**, *36*, 3632.

Figures 5 and 6 provide the key to the understanding of the change in J in the LF excited states of μ-O,Me$_3$tacn. As illustrated in Figure 6 (center) $yz \rightarrow z^2$ excitation (band I, Figure 2) converts the antiferromagnetic Mn1(yz)−O−Mn2(yz) pathway into a ferromagnetic pathway and "turns on" the Mn1 z^2-based, mixed σ/π Mn1(z^2)−O−Mn2(xz) antiferromagnetic superexchange pathway. (Note that the proper dimer wave functions correspond to the symmetric and antisymmetric combinations of the locally excited configurations, see Figure 3.) Since the number of ferromagnetic and antiferromagnetic superexchange pathways remains unchanged upon $yz \rightarrow z^2$ excitation (cf. Figure 6, left and center), the experimental J[B$_2$(yz)] value of −55 cm^{-1} obtained from the variable temperature behavior of band I indicates that the Mn1(z^2)−O−Mn2(xz) pathway is more efficient in mediating exchange coupling than the symmetric Mn1(yz)−O−Mn2(yz) pathway, consistent with the larger Mn2 d-orbital character calculated for the former (Figure 5, Table 1).

Upon $xz \rightarrow z^2$ excitation (band II), the ferromagnetic Mn1(xz)−O−Mn2(z^2) pathway and its Mn2-based counterpart are eliminated, while the Mn1 z^2-based antiferromagnetic superexchange pathway is "switched on" (Figure 6, right). The antiferromagnetic Mn1(yz)−O−Mn2(yz) pathway is maintained, whereas the Mn1(xz)−O−Mn2(xz) pathway turns into a ferromagnetic pathway. Consequently, the strong antiferromagnetic exchange coupling in the $^{2S+1}$A$_1$(xz) excited state, J[A$_1$(xz)] = −165 cm^{-1}, is a direct experimental manifestation of the dominance of the mixed π/σ Mn(xz)−O−Mn(z^2) superexchange pathway in μ-O,Me$_3$tacn.

In summary, the weak ferromagnetic exchange coupling in the ground state of μ-O,Me$_3$tacn arises from a balance between ferromagnetic and antiferromagnetic contributions to J (Figure 6, left). In the $^{2S+1}$B$_2$(yz) and $^{2S+1}$A$_1$(xz) LF excited states this balance is perturbed in favor of antiferromagnetic contributions because one of the mixed π/σ Mn(xz)−O−Mn(z^2) superexchange pathways now produces a large antiferromagnetic contribution to J (Figure 6, center and right). These results indicate that the relative importance of the major antiferromagnetic superexchange pathways in μ-O,Me$_3$tacn is $|J_{xz/z^2}| > |J_{yz/yz}| > |J_{xz/xz}|$ where xz and yz are, respectively, the Mn−O−Mn in-plane and out-of-plane manganese d-based orbitals.

Excited-State Contributions to the Ground-State Exchange Coupling. The results presented above demonstrate that the weak ground-state exchange coupling in μ-O,Me$_3$tacn arises from a near cancellation of ferromagnetic and antiferromagnetic contributions to J rather than from the lack of efficient superexchange pathways (Figure 6). In the framework of the Anderson theory of superexchange, ground-state exchange coupling arises from configuration interaction (CI) mixing of the ground state with metal-to-metal charge transfer (MMCT) excited states.[41−43] In the present case antiferromagnetic contributions to J arise from CI mixing with MMCT excited states in which an electron has been promoted from a singly occupied d orbital on one manganese to any of the five d orbitals on the second manganese, such that the resulting Mn(II) ion is in an $S = {}^{3}/_{2}$ excited state (Chart 2, top left). Alternatively, ferromagnetic contributions originate from CI mixing with MMCT states in which an electron from a singly occupied d orbital on one Mn center has been transferred to the sole unoccupied d orbital on the second Mn, formally producing a ground state $S = {}^{5}/_{2}$ Mn(II) center (Chart 2, top right).[42] Although these states are lower in energy than the MMCT excited states contributing to antiferromagnetic coupling by ~25000 cm^{-1} (estimated from the spin flip energy for octahedral Mn(II) complexes[33,44]), the stabilization is small compared to the MMCT excitation energy for which we estimate a value of ~75000 cm^{-1}. Thus, given the substantially larger number of possible antiferromagnetic vs ferromagnetic contributions to J, the weak ferromagnetic coupling in the ground state of μ-O,Me$_3$tacn observed experimentally is difficult to rationalize in terms of the Anderson superexchange model.

Chart 2. Representative Electronic Configurations for the VBCI Analysis

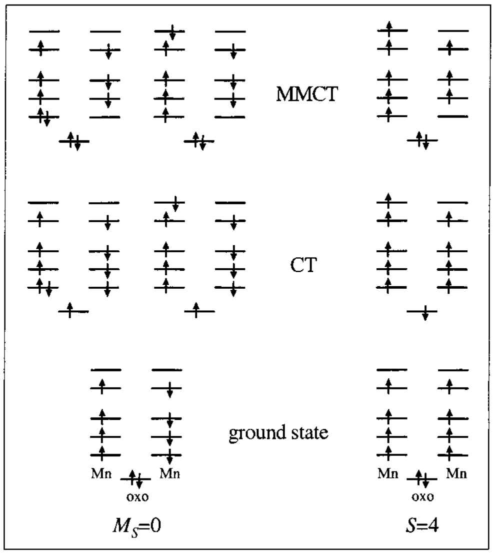

Insight into the origin of this ferromagnetic coupling can be obtained by employing the recently developed valence bond configuration interaction (VBCI) model.[20,21,45,46] In the VBCI formalism ground-state exchange coupling is described as arising from CI mixing of MMCT excited states into the oxo-to-Mn CT excited states that in turn interact with the ground state (we do not include double CT excited states here as these are high in energy and will not significantly contribute to exchange coupling in μ-Me$_3$tacn[47]). The relevant part of the Hamiltonian responsible for this CI mixing is composed of one-electron and two-electron terms that account for the interaction of the two monomer halves in the dimer. Because the two-center two-electron exchange integrals are only on the order of 1−10 cm^{-1} the VBCI matrix elements can be evaluated solely for the one-electron operator, $\hat{h}$, and CI will only occur between states arising from electronic configurations that differ by no more than one electron.[21] Representative CT electron configurations leading to antiferromagnetic ($M_S = 0$) and ferromagnetic ($S = 4$) contributions to J are illustrated in Chart 2 (middle left and right, respectively).

To evaluate the VBCI matrix elements, the many-electron wave functions for the ground state and the CT and MMCT excited states were expressed in terms of Slater determinants using Clebsch−Gordan coefficients.[48] The wave functions for the antiferromagnetically ($S = 0$) and ferromagnetically coupled

---

(43) (a) Anderson, P. W. *Phys. Rev.* **1959**, *115*, 2. (b) Anderson, P. W. In *Magnetism;* Rado, G. T., Suhl, H., Eds.; Academic Press: New York, 1963; Vol. 1, Chapter 2.

(44) Solomon, E. I.; McClure, D. S. *Phys. Rev. B* **1974**, *9*, 4690.

(45) Tuczek, F.; Solomon, E. I. *J. Am. Chem. Soc.* **1994**, *116*, 6916.

(46) Tuczek, F. In *Spectroscopic Methods in Bioinorganic Chemistry;* Solomon, E. I., Hodgson, K. O., Eds.; ACS Symposium Series 692; American Chemical Society: Washington, DC, 1997; pp 98−118.

(47) In other dimers DCT excited states can also make a contribution to ground-state exchange coupling.[20,21,45,46]

(48) Rotenberg, M.; Bivins, R.; Metropolis, N.; Wooten, J. K., Jr. *The 3-j and 6-j Symbols;* The Technology Press: Cambridge, MA, 1959.

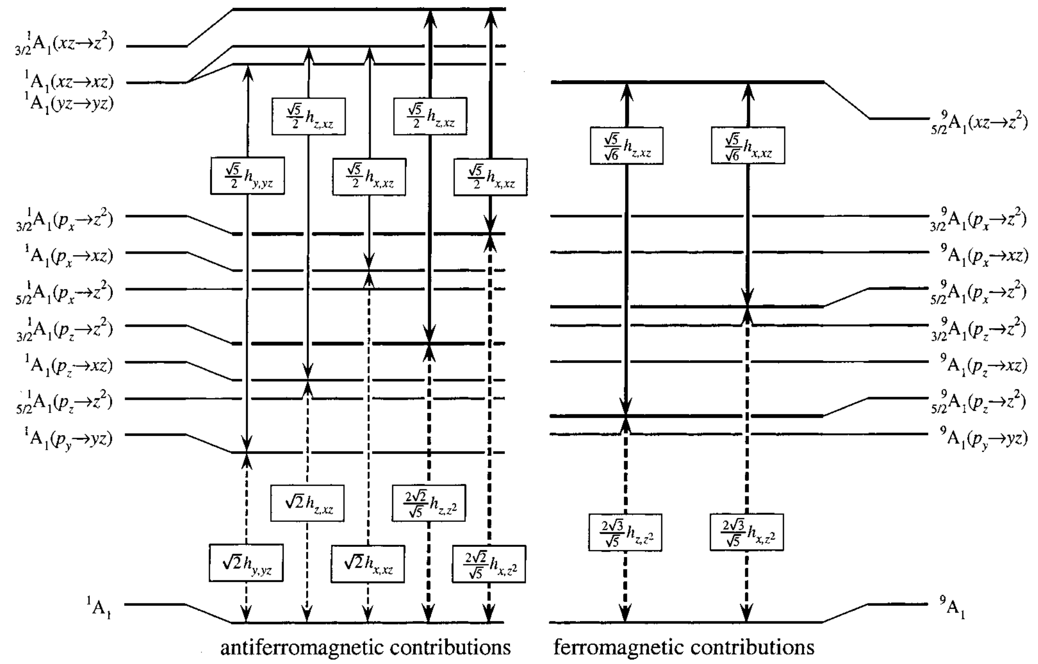

Figure 7. VBCI analysis of exchange coupling in the ground state of μ-O,Me$_3$tacn. The effects of CI mixing of the relevant $S = 0$ and $S = 4$ ground and CT excited states with metal-to-metal CT excited states are shown on the left and on the right, respectively. Only superexchange pathways that contribute to the ground-state exchange splitting (in fourth order) are shown. Note that CI between the ground state and the CT excited states is spin independent and thus results in an equal stabilization of all ground-state spin sublevels (on the far left and right this second-order CI mixing is already included). The relative ordering of the CT excited states is based upon the MO energies obtained from a HS ($S = 4$) DFT calculation on μ-O,Me$_3$tacn. CI matrix elements are expressed in terms of one-electron transfer integrals.

($S = 4$) dimer ground states are given in Table S2 (Supporting Information). Since both the $S = 0$ and $S = 4$ components of the ground state transform as A_1 (Figure 3), they can only interact with states arising from the symmetric combinations of the locally excited CT and MMCT configurations that also transform as A_1. Further, because the transfer integrals approximately scale with the Mn−oxo orbital overlap[49] only a subset of all possible CI matrix elements need to be considered (cf. Figure 5, Table 1). The relevant matrix elements expressed in terms of transfer integrals are given in the schematic VBCI energy level diagram in Figure 7. For example, the VBCI matrix element between the ${}^9\mathrm{A}_1$ ground state and the $_{5/2}{}^9\mathrm{A}_1^{CT}(p_z \rightarrow z^2)$ CT excited state in which an electron has been promoted from the oxo p$_z$ orbital into the Mn z^2 orbital producing an $S = {}^5/_2$ Mn(II) center is written as follows:

$$\langle{}^9\mathrm{A}_1^{CT}|\hat{h}\,|{}_{5/2}{}^9\mathrm{A}_1(\mathrm{p}_z \rightarrow z^2)\rangle = \frac{2\sqrt{3}}{\sqrt{5}}\langle p_z|\hat{h}\,|z^2\rangle \equiv \frac{2\sqrt{3}}{\sqrt{5}}h_{z,z^2} \quad (1)$$

Using fourth-order perturbation theory, the following expression is obtained for the ground state J value:[46]

$$n(n+1)\,J = \sum_i \lambda_i^2\left[\sum_k \frac{|\langle{}^9\mathrm{A}_1^{CT}|\hat{h}\,|{}^9\mathrm{A}_1^{MMCT,k}\rangle|^2}{E({}^9\mathrm{A}_1^{MMCT,k}) - E({}^9\mathrm{A}_1)} - \sum_l \frac{|\langle{}^1\mathrm{A}_1^{CT,i}|\hat{h}\,|{}^1\mathrm{A}_1^{MMCT,l}\rangle|^2}{E({}^1\mathrm{A}_1^{MMCT,l}) - E({}^1\mathrm{A}_1)}\right] \quad (2)$$

where n is the number of unpaired electrons per Mn(III) center ($n = 4$) and the summation is carried out over all CT excited states, ${}^{2S+1}\mathrm{A}_1^{\mathrm{CT},i}$, and MMCT excited states, ${}^9\mathrm{A}_1^{MMCT,k}$ and ${}^1\mathrm{A}_1^{MMCT,l}$. The relevant matrix elements are given in Figure 7, and the first order mixing coefficients are defined as follows:

$$\lambda_i = \frac{\langle{}^{2S+1}\mathrm{A}_1|\hat{h}\,|{}^{2S+1}\mathrm{A}_1^{CT,i}\rangle}{E({}^{2S+1}\mathrm{A}_1) - E({}^{2S+1}\mathrm{A}_1^{CT,i})} \quad (3)$$

These coefficients are spin-independent, and CI mixing with LMCT excited states thus leads to an equal stabilization of all spin sublevels of the dimer ground state (cf. Figure 7, far left and right for the $2S + 1 = 1$ and 9 states, respectively). This degeneracy is removed through spin-dependent fourth-order mixing with MMCT excited states (eq 2), however. From eqs 2 and 3 the effect of excited-state antiferromagnetism due to CI between MMCT and CT excited states upon the ground state J value is inversely proportional to the square of the energy difference between the ground state and the CT excited state serving as the intermediate level for CI with MMCT excited states. As presented in the previous sections the mixed π/σ Mn−O−Mn pathways (bold arrows in Figure 7) are the most efficient superexchange pathways in μ-O,Me$_3$tacn. Significantly, antiferromagnetic contributions associated with these pathways involve the CT excited states in which the Mn(II) center is in an $S = {}^3/_2$ excited state, whereas ferromagnetic contributions involve CT excited states in which the Mn(II) center is in its $S = {}^5/_2$ ground state that is ~25000 lower energy due to a large single-center exchange stabilization (*vide supra*). The corresponding energy denominators in eq 3 thus differ by $\Delta E = E({}_{3/2}{}^1\mathrm{A}_1^{CT}) - E({}_{5/2}{}^9\mathrm{A}_1^{CT}) \approx 25000\ \mathrm{cm}^{-1}$. Using eqs 2 and 3 with the matrix elements in Figure 7, the ratio of the ferromagnetic vs antiferromagnetic contributions to the ground-state exchange coupling from the mixed π/σ Mn−O−Mn superexchange pathways is roughly $([E({}_{5/2}{}^9\mathrm{A}_1^{CT}) + \Delta E]/[E({}_{5/2}{}^9\mathrm{A}_1^{CT})])^2 \times ([E({}_{5/2}{}^9\mathrm{A}_1^{MMCT}) + \Delta E]/[E({}_{5/2}{}^9\mathrm{A}_1^{MMCT})]) \approx 3{-}5$ (cf. Figure S2, Supporting Information), substantially larger than would be

---

[49] Wolfsberg, M.; Helmholz, L. *J. Chem. Phys.* **1955**, *23*, 1841.

expected on the basis of the Anderson superexchange model ($[E({}_{5/2}{}^{9}\mathrm{A}_1^{MMCT}) + \Delta E]/[E({}_{5/2}{}^{9}\mathrm{A}_1^{MMCT})] \approx 1-1.5$). From the experimentally observed ferromagnetic ground-state exchange coupling in μ-O,Me$_3$tacn, the ferromagnetic contribution to J associated with the mixed pathway is sufficiently large to offset all antiferromagnetic contributions.

Efficiency of Superexchange Pathways for Electron Transfer. Two-electron transfer from a binuclear metal center can be an important step in the catalytic cycle of metalloproteins. In these processes the rate constant for the transfer of the second electron will strongly depend on the strength of electronic coupling between the two metals, H_{AB}. For typical metal−metal distances the direct interaction is negligible, and electronic coupling is mediated by intervening bridges *via* superexchange.[50] Consequently, the superexchange pathways that produce the dominant contributions to the ground-state exchange coupling constant J should also contribute most to the rate constant for intramolecular metal−metal electron transfer (ET), and analysis of the orbital origin of exchange coupling could provide insight into the dominant ET pathways. A complication in this analysis relates to the fact that the ET step typically involves a mixed valence (MV) state of the binuclear site. While in this case the formalism developed by Hush[51] can in principle be employed to estimate H_{AB} from the intensity of the intervalence transfer absorption band, the catalytically relevant MV species are often difficult to study directly (*vide infra*). Further, in paramagnetic MV dimers it is difficult to correlate the calculated H_{AB} with an individual superexchange pathway because of the complex interplay between electron exchange and double exchange.[52] Therefore, a convenient approach would involve (i) determination of the H_{AB} value for a superexchange pathway from its contributions to J in the homovalent site and (ii) appropriate scaling of this value for the MV species. This approach is presented here employing the VBCI model. First, the contribution from an individual superexchange pathway to J of a homovalent dimer is used to estimate the value of H_{AB} in the homovalent case. This value is then correlated with the electronic coupling matrix element H_{AB}^{MV} for the one-electron reduced MV analogue.

The homovalent model system used consists of two metal centers (A and B), each possessing a single half-occupied orbital (d_A and d_B), and a diamagnetic bridging ligand. In this case there are no triplet MMCT excited states, and only the singlet states need to be considered. The zeroth-order singlet ground state determinantal wave function is:

$$^{1}\mathrm{A}_1^{GS} = \frac{1}{\sqrt{2}}(|d_A L\bar{L}\bar{d}_B| - |\bar{d}_A L\bar{L} d_B|) \quad (4)$$

The ligand-to-metal CT excited state of proper symmetry for interaction with the ground state arises from the symmetric combination of the locally excited $L \rightarrow d_A$ and $L \rightarrow d_B$ configurations:

$$^{1}\mathrm{A}_1^{CT} = \frac{1}{2}(|d_A L\bar{d}_A\bar{d}_B| - |d_A\bar{L}\bar{d}_A d_B| + |d_A d_B\bar{L}\bar{d}_B| - |\bar{d}_A d_B L\bar{d}_B|) \quad (5)$$

Similarly, the relevant MMCT excited-state derives from the symmetric combination of the $d_B \rightarrow d_A$ and $d_A \rightarrow d_B$ configurations:

$$^{1}\mathrm{A}_1^{MMCT} = \frac{1}{\sqrt{2}}(|d_A L\bar{L}\bar{d}_A| + |d_B L\bar{L}\bar{d}_B|) \quad (6)$$

With these wave functions the following CI matrix elements are obtained:[53]

$$\langle {}^{1}\mathrm{A}_1^{GS}|\hat{h}\,|{}^{1}\mathrm{A}_1^{CT}\rangle = \langle {}^{1}\mathrm{A}_1^{CT}|\hat{h}\,|{}^{1}\mathrm{A}_1^{MMCT}\rangle = \sqrt{2}\langle L|\hat{h}\,|d\rangle \equiv \sqrt{2}h_{LD} \quad (7)$$

where the direct exchange term $\langle {}^{1}\mathrm{A}_1^{GS}|\hat{h}\,|{}^{1}\mathrm{A}_1^{MMCT}\rangle \approx 0$ due to the lack of overlap between d_A and d_B.

The key parameter defining the efficiency of a superexchange pathway for electron transfer is the electronic coupling matrix element, H_{AB}.[54,55] By defining $U = E({}^{1}\mathrm{A}_1^{MMCT}) - E({}^{1}\mathrm{A}_1^{GS})$ and $\Delta = E({}^{1}\mathrm{A}_1^{CT}) - E({}^{1}\mathrm{A}_1^{GS})$ to second order the MMCT→ GS mixing coefficient c_{AB} is approximately given by:[56]

$$c_{AB} = \frac{H_{AB}}{U} = \frac{1}{U}\left(\langle {}^{1}\mathrm{A}_1^{GS}|\hat{h}\,|{}^{1}\mathrm{A}_1^{MMCT}\rangle + \frac{\langle {}^{1}\mathrm{A}_1^{GS}|\hat{h}\,|{}^{1}\mathrm{A}_1^{CT}\rangle\langle {}^{1}\mathrm{A}_1^{CT}|\hat{h}\,|{}^{1}\mathrm{A}_1^{MMCT}\rangle}{\Delta}\right) \cong \frac{2(h_{Ld})^2}{U\Delta} \quad (8)$$

Thus, the electronic coupling matrix element becomes:

$$H_{AB} = c_{AB}U = \frac{2(h_{Ld})^2}{\Delta} \quad (9)$$

Alternatively, using eqs 2 and 3 the following expression is obtained for the ground-state exchange coupling constant:

$$-2J = \frac{2(h_{Ld})^2}{\Delta^2}\left[\frac{2(h_{Ld})^2}{U}\right] = \frac{(H_{AB})^2}{U} \quad (10)$$

For a homobinuclear dimer with more than one unpaired electron $n_A = n_B = n$ on each metal center, eq 10 can be modified to express the contribution $J_{a/b}$ from a superexchange pathway involving orbital a on center A and orbital b on B to J in terms of the corresponding electronic coupling matrix element $H_{A_aB_b}$ as follows:

$$-J_{a/b} = \frac{1}{n(n+1)}\frac{(H_{A_aB_b})^2}{U} \quad (11)$$

or $(H_{A_aB_b})^2 = -n(n+1)J_{a/b}U$. This gives the very important result that for a homovalent dimer the value of $J_{a/b}$ can be used to estimate the value of the electronic coupling matrix element $H_{A_aB_b}$ if a reasonable estimate of the MMCT energy U is available (e.g., from photoelectron spectroscopic studies on $\mathrm{CuCl_4}^{2-}$,[57] a value of $U \approx 53000$ cm^{-1} would be appropriate for Cu(II)$_2$ dimers). Note that from the VBCI model for a pathway involving a singly occupied orbital on A and an unoccupied orbital on B the net (ferromagnetic) contribution

---

(50) An example of a binuclear metalloprotein site that does have a direct metal−metal interaction is the Cu$_A$ ET center in cytochrome *c* oxidase. (a) Gamelin, D. R.; Randall, D. W.; Hay, M. T.; Houser, R. P.; Mulder, T. C.; Canters, G. W.; Devries, S.; Tolman, W. B.; Lu, Y.; Solomon, E. I. *J. Am. Chem. Soc.* **1998**, *120*, 5246. (b) Solomon, E. I.; Randall, D. W.; Glaser, T. *Coord. Chem. Rev.* **2000**, *200*, in press.

(51) Hush, N. S. *Electrochim. Acta* **1968**, *13*, 1005.

(52) Bolondin, G.; Girerd. J.-J. *Chem. Rev.* **1990**, *90*, 1359.

(53) Note that $\sqrt{2}h_{Ld}$ in eq 7 was redefined as $h_{d\pi}$ in refs 21, 20, and 46.

(54) Newton, M. D. *Chem. Rev.* **1991**, *91*, 767 and references therein.

(55) Barbara, P. F.; Meyer, T. J.; Ratner, M. A. *J. Chem. Phys.* **1996**, *100*, 13148 and references therein.

(56) Richardson, D. E.; Taube, H. *J. Am. Chem. Soc.* **1983**, *105*, 40.

(57) Didziulis, S. V.; Cohen, S. L.; Gewirth, A. A.; Solomon, E. I. *J. Am. Chem. Soc.* **1988**, *110*, 250.

to *J* actually has antiferromagnetic and ferromagnetic contributions, $J_{a/b}^{af} - J_{a/b}^{f}$ (cf. eq 2 and Figure 7). In this case the value of $(H_{A_aB_b})^2$ is spin-dependent and can be estimated from $J_{a/b}^{af}$ and $J_{a/b}^{f}$.[58]

As mentioned above, metal−metal ET reactions in metalloproteins typically proceed through the MV state of binuclear metalloproteins. To explore how H_{AB} changes upon one-electron reduction of the dimer, an electron is added to metal A of the model dimer used in the derivation of eq 10. The corresponding $S = {}^1/_2$ ($M_S = +{}^1/_2$) ground state, CT excited state, and MMCT excited-state wave functions are given by:

$$^2\Psi^{GS} = |d_A\bar{d}_AL\bar{L}d_B| \tag{12}$$

$$^2\Psi^{CT} = |d_A\bar{d}_AL\bar{d}_Bd_B| \tag{13}$$

$$^2\Psi^{MMCT} = |d_A\bar{L}L\bar{d}_Bd_B| \tag{14}$$

and the CI matrix elements are:

$$\langle {}^2\Psi^{GS}|\hat{h}\,|{}^2\Psi^{CT}\rangle = h_{Ld}; \quad \langle {}^2\Psi^{CT}|\hat{h}\,|{}^2\Psi^{MMCT}\rangle\, h'_{Ld} \tag{15}$$

h'_{Ld} is the resonance integral involving the reduced center A. It may be similar in magnitude to h_{Ld} because the effect of the more diffuse d orbital on the reduced site, which would tend to increase h'_{Ld}, is offset by the longer A−L bond distance. Using eqs 8 and 9 and assuming that the energy of the L→ B CT transition Δ does not change upon reduction of A, the following expression for the electronic coupling matrix element in the MV dimer is obtained:

$$H_{AB}^{MV} = \frac{1}{2}\frac{h'_{Ld}}{h_{Ld}}H_{AB} \cong \frac{1}{2}H_{AB} \tag{16}$$

where the reduction of H_{AB}^{MV} from H_{AB} by ∼2 is due to the loss of the 2-fold symmetry in the MV dimer, which eliminates the factor of $\sqrt{2}$ in the CI matrix elements (cf. eqs 7 and 15). From eqs 11 and 16 the *J* value obtained for the homovalent dimer can be used to estimate H_{AB}^{MV} for its one-electron reduced MV analogue. This approach should be particularly useful for calculating H_{AB}^{MV} from the *J* value of homovalent dimers possessing a single unpaired electron on each metal (e.g., Cu(II)$_2$ dimers and low-spin Ru(III)$_2$ dimers) because in this case all superexchange pathways contributing to *J* in the oxidized dimer may serve as ET pathways in the MV analogue.[59] The same formalism can be used to estimate H_{AB}^{MV} for one-electron oxidized MV dimers; however, in this case the ligand-to-metal CT transition energy, Δ′, will typically be smaller than Δ, and a factor of Δ/Δ′ must be included in eq 16.

From eqs 9 and 11 both H_{AB} and *J* depend on the transfer integral h_{Ld}. An approximate value for this integral can be obtained from the CT absorption spectrum. The transition moment integral for an L→ M CT transition is approximately given by[60] $\mu_{CT} \approx c_L^M R_{M-L}$ where c_L^M is the coefficient of the ligand orbital in the metal-based acceptor MO and R_{M-L} is the metal−ligand bond length (in Å). In the VBCI formalism bonding is introduced through CI, and the value of c_L^M can be estimated from the ratio of the corresponding resonance integral (eq 7) and the CT energy, $c_L^M = \sqrt{2}h_{Ld}/\Delta$. Hence:[61,62]

$$\mu_{CT} \approx \frac{\sqrt{2}h_{Ld}R_{M-L}}{\Delta} \tag{17}$$

where μ_{CT} is in units of eÅ. With the theoretical expression for the oscillator strength, $f = 1.085 \times 10^{-5}\Delta(\mu_{CT})^2$, h_{Ld} can be estimated from the CT absorption spectrum:

$$(h_{Ld})^2 \approx 46 \times 10^3 \frac{f\Delta}{(R_{M-L})^2} \tag{18}$$

where *f* can be determined experimentally, $f = 4.32 \times 10^{-9} \int\epsilon(\nu)\mathrm{d}\nu$.[63] Analysis of the CT absorption spectrum can thus provide significant insight into the orbital origin of ground-state exchange coupling because the dominant superexchange pathways will give rise to intense, low-energy absorption features (i.e., small Δ and large $(h_{Ld})^2$, cf. eqs 2, 3, and 18).

4. Discussion

Efficiency of Superexchange Pathways in Oxo-Bridged Mn(III)$_2$ Dimers. In the present study an excited-state spectroscopic approach was used to experimentally evaluate the efficiency of individual superexchange pathways in the homobinuclear oxo-bridged Mn(III)$_2$ dimer [Mn(III)$_2$O(OAc)$_2$(Me$_3$-tacn)$_2$]$^{2+}$ (referred to as μ-O,Me$_3$tacn). Quantitative analysis of the temperature effects in the corresponding polarized single-crystal electronic absorption spectra (Figure 2) leads to estimates for the exchange coupling constants in the excited states corresponding to bands *I* and *II* of $J[\mathrm{B}_2(yz)] = -55$ cm^{-1} and $J[\mathrm{A}_1(xz)] = -165$ cm^{-1}, respectively. The large changes in *J* upon d → d excitation of μ-O,Me$_3$tacn are understood on the basis of the schemes in Figure 6 and indicate that $|J_{xz,z^2}| > |J_{yz,yz}| > |J_{xz,xz}|$, in agreement with the calculated MO descriptions (Figure 5, Table 1). The high efficiency of mixed π/σ Mn(*xz*)−O−Mn(z^2) superexchange pathway arises from the substantial metal−ligand covalency of the z^2 and *xz* orbitals with the same oxo *p* orbital. This covalency governs the magnitude of the transfer integrals responsible for CI mixing of MMCT excited states into the ground state *via* intermediate CT excited states involving the oxo bridge (Figure 7).

In Figure 6 left an increase in Mn−O−Mn angle, γ, toward a linear geometry will lower the ferromagnetic contributions to *J* by reducing the Mn2 z^2-orbital character in the Mn1 *xz*-based MO (in the linear limit this pathway is eliminated by symmetry). Concomitantly, the antiferromagnetic contribution associated with the symmetric Mn1(*xz*)−O−Mn2(*xz*) pathway will increase; i.e., $J_{xz/xz}$ approaches $J_{yz/yz}$. Thus, an increase in γ would be expected to result in an increase in antiferromagnetic contributions to *J* at the expense of ferromagnetic contributions, consistent with the strong antiferromagnetic exchange coupling in the ground state of a nearly linear (γ = 168°, *r*(Mn−O) = 1.76 Å) oxo-bridged Mn(III)$_2$ dimer, $J = -120$ cm^{-1}.[12]

In the framework of the VBCI model, one of the two matrix elements responsible for second-order CI mixing of the ${}_{5/2}{}^9\mathrm{A}_1^{MMCT}$ excited state into the ${}^9\mathrm{A}_1$ ground state (Figure 7,

---

[58] If the model dimer used in the derivation of eq 10 is expanded by a single unoccupied orbital on each metal, the net ferromagnetic contribution to *J* involving this orbital is $2J_{a/b} = (H_{A_aB_b}^{f})^2/U^f - (H_{A_aB_b}^{af})^2/U^{af}$ where $H_{A_aB_b}^{f}/H_{A_aB_b}^{af} = \Delta^{af}/\Delta^f$ and $U^{af} - U^f \approx \Delta^{af}/\Delta^f \approx 10000$ cm^{-1}, corresponding to the spin flip-energy on the one-electron reduced metal center (a d^2 ion) in the MMCT excited state.

[59] In MV dimers with low-lying metal-to-ligand CT excited states additional superexchange pathways for intramolecular metal−metal ET may exist.

[60] Baldwin, M. J.; Root, D. E.; Pate, J. E.; Fujisawa, K.; Kitajima, N.; Solomon, E. *J. Am. Chem. Soc.* **1992**, *114*, 10421.

[61] Mayoh, B.; Day, P. *Inorg. Chem.* **1974**, *13*, 2273.

[62] For a L→ M CT transition in a monomer involving a doubly occupied ligand orbital and a singly occupied metal orbital the $\sqrt{2}$ in eq 17 disappears.

[63] Solomon, E. I. *Comments Inorg. Chem.* **1984**, *3*, 225.

right) vanishes for $\gamma = 180°$ due to the lack of orbital overlap of the oxo $p_{z'}$ and $p_{x'}$ orbitals with the Mn z^2 and *xz* orbitals, respectively (cf. Chart 1 for axes orientations). Thus, the $S = 4$ ground state component in the nearly linear dimer is not subject to CI with MMCT excited states, and the experimental splitting between the $S = 0$ and $S = 4$ states in that dimer, $-20J = 2400$ cm^{-1}, provides a direct measure of the singlet ground-state stabilization due to superexchange involving the symmetric π/π Mn(*xz*)−O−Mn(*xz*) and Mn(*yz*)−O−Mn(*yz*) pathways (Figure 7, left). Upon bending of the Mn−O−Mn unit in μ-O,Me$_3$tacn ($\gamma = 120°$), the former contribution decreases due to a reduction of the $h_{x,xz}$ transfer integral (i.e., a decrease in orbital overlap), whereas the latter contribution remains essentially unchanged. Because of an additional antiferromagnetic contribution in the bent dimer associated with mixed π/σ Mn−O−Mn superexchange pathways, the total stabilization of the $^1A_1$ ground state likely remains greater than 2000 cm^{-1}. Given the weak ferromagnetic coupling in μ-O,Me$_3$tacn observed experimentally, the $^9A_1$ ground state is therefore stabilized by at least 2000 cm^{-1} due to second-order CI with the $_{5/2}{}^{9}A_1^{MMCT}$ excited state. From eq 11 with an estimated value for U of 70000−75000 cm^{-1} this gives $|H_{xz/z^2}| \approx 12000$ cm^{-1} for the electronic coupling matrix element associated with the mixed π/σ pathways. The significance of this result for the reactivities of binuclear metalloproteins will be discussed below.

Excited-State Magneto-Structural Correlations. Identification of oxo-bridges at the active sites of binuclear non-heme iron proteins and in synthetic diferric model complexes is greatly facilitated by the characteristic magnetic and spectral features inherent to the Fe(III)−O−Fe(III) core.[4] In particular, discrimination between μ-O and μ-OH bridged structures is readily achieved on the basis of the large differences in ground-state exchange coupling constants, $J \approx -120$ and -15 cm^{-1}, respectively.[4] Alternatively, in bent Mn(III)$_2$ dimers, cancellation of ferromagnetic and antiferromagnetic contributions to J (Figure 6) produce a weakly exchange-coupled ground state even in the presence of an oxo bridge.[2] Further, identification of unique spectral features in the electronic absorption spectrum of oxo-bridged Mn(III)$_2$ complexes is rather elusive. Although the high covalency of the Mn−O−Mn bond gives rise to unusually high absorption intensity in the LF region of Mn(III)$_2$ dimers possessing six-coordinate metal centers,[26] five-coordinate Mn(III) complexes typically exhibit similarly strong d → d absorption bands.[33−35]

From our recent low-temperature spectroscopic studies of μ-O,Me$_3$tacn and related oxo-bridged Mn(III)$_2$ complexes we found[26,27] that band *I* (Figure 1), which is very prominent in the MCD spectra of all the dimers studied, may serve as a useful spectroscopic probe for the presence of an oxo bridge because its low energy and high absorption intensity derive from the unusually strong antibonding interaction of the Mn *yz* orbital with the out-of plane oxo $p_{y'}$ orbital (Figure 5, center). The results obtained in the present study suggest a complementary approach for probing the presence of an oxo bridge at binuclear Mn(III)$_2$ sites. In oxo-bridged dimers, thermal population of low-lying ground-state spin sublevels with increasing temperature between 5 and 300 K will give rise to significant changes in the absorption spectrum due to the large antiferromagnetic energy splittings in the ligand-field excited states (Figures 2 and S1). Alternatively, because of the poor efficiency of a hydroxo bridge in mediating superexchange, the absorption spectrum of an OH-bridged Mn(III)$_2$ dimer should be essentially temperature-independent. Thus, by investigating the temperature dependence of the electronic absorption spectrum, discrimination between oxo- and hydroxo-bridged Mn(III)$_2$ core structures should be possible. This approach has been applied to oxidized Mn(III)$_2$ catalase for which both oxo- and hydroxo-bridged structures have been proposed.[26,65,66] The variable-temperature absorption data show no change in band positions or intensities between 5 and 300 K, consistent with the assignment of the bridging ligand as μ-OH.[67]

Extension to Oxo-Bridged Binuclear Non-Heme Iron Proteins. The multiply-bridged μ-oxo diiron(III) structural motif occurs in several metalloproteins whose functions involve reversible binding or activation of dioxygen.[1,68−70] In an early step of these processes each ferrous ion of the reduced binuclear site transfers one electron to dioxygen, yielding a diiron(III) peroxide species. If both Fe(II) centers possess an open coordination site, a bridging μ-1,2 binding mode of O$_2$, as proposed for several dioxygen activating enzymes including methane monooxygenase,[69,71] ribonucleotide reductase,[72] and Δ^9 stearoyl-acyl carrier protein desaturase,[73] can afford large electronic coupling to both irons and eliminate the need for a good electron-transfer (ET) pathway between the two metal centers.[74] In the case of the dioxygen carrier protein hemerythrin (Hr), however, only one Fe(II) center of the μ-OH bridged diferrous active site (deoxyHr) has an open coordination position.[18] In the oxygenation process of deoxyHr, one electron from each Fe(II) and the proton from the bridging hydroxide are transferred to O$_2$ binding to a single metal center, yielding a terminal hydroperoxide at the oxo-bridged diferric site of oxyHr.[18] On the basis of electronic structure calculations we proposed that the ET from the six-coordinate Fe(II) center (Fe2) to dioxygen binding to the other Fe(II) center (Fe1) is coupled to the proton transfer and occurs through the mixed π/σ Fe(*xz*)−O−Fe(z^2) superexchange pathway (Figure 8A, top).[17] An appealing feature of this putative ET pathway relates to the fact that it should afford large electronic coupling between the O$_2$ π^* orbital involved in a σ-bonding interaction with Fe1 and the redox-active, π-antibonding d orbital on Fe2 (Figure 8A, bottom).

Given the fact that the calculated metal d orbital compositions and M−O−M core structures for μ-O,Me$_3$tacn, its Fe(III) analogue,[20,64] and oxyHr[16] are very similar, it appears reasonable to assume that the value of $|H_{xz,z^2}| \approx 12000$ cm^{-1} obtained for μ-O,Me$_3$tacn is roughly similar in these dimers. Since the proton-coupled ET (PCET) in the process of O$_2$ binding to deoxyHr formally involves an oxo-bridged Fe2(II)/Fe1(III)

---

(64) Brunold, T. C.; Tamura, N.; Kitajima, N.; Moro-oka, Y.; Solomon, E. I. *J. Am. Chem. Soc.* **1998**, *120*, 5674.

(65) Dismukes, G. C. *Chem. Rev.* **1996**, *96*, 2909.

(66) Whittaker, M. M.; Barynin, V. V.; Antonyuk, S. V.; Whittaker, J. *Biochemistry* **1999**, *38*, 9126.

(67) Brunold, T. C.; Gamelin, D. R.; Yoder, D.; Penner-Hahn, J.; Solomon, E. I. Manuscript in preparation.

(68) Feig, A. L.; Lippard, S. J. *Chem. Rev.* **1994**, *94*, 759.

(69) Wallar, B. J.; Lipscomb, J. D. *Chem. Rev.* **1996**, *96*, 2625.

(70) Solomon, E. I.; Brunold, T. C. Davis, M. I.; Kemsley, J. N.; Lee, S.-K.; Lehnert, N.; Neese, F.; Skulan, A.-J.; Yang, Y.-S.; Zhou, J. *Chem. Rev.* **2000**, *100*, 235−349.

(71) (a) Lee, S.-K.; Nesheim, J. C.; Lipscomb, J. D. *J. Biol. Chem.* **1993**, *268*, 21569. (b) Liu, K. E.; Valentine, A. M.; Wang, D.; Huynh, B. H.; Edmondson, D. E.; Salifoglou, A.; Lippard, S. J. *J. Am. Chem. Soc.* **1995**, *117*, 10174.

(72) (a) Tong, W. H.; Chen, S.; Lloyd, S. G.; Edmondson, D. E.; Huynh, B. H.; Stubbe, J. *J. Am. Chem. Soc.* **1996**, *118*, 2107. (b) Bollinger, J. M., Jr.; Krebs, C.; Vicol, A.; Chen, S.; Ley, B. A.; Edmondson, D. E.; Huynh, B. H. *J. Am. Chem. Soc.* **1998**, *120*, 1094. (c) Moënne-Loccoz, P.; Baldwin, J.; Ley, B. A.; Loehr, T. M.; Bollinger, J. M., Jr. *Biochemistry* **1998**, *37*, 14659.

(73) Broadwater, J. A.; Ai, J.; Loehr, T. M.; Sanders-Loehr, J.; Fox, B. G. *Biochemistry* **1998**, *37*, 14664.

(74) Yang, Y.-S.; Baldwin, J.; Ley, B. A.; Bollinger, J. M., Jr.; Solomon, E. I., submitted.

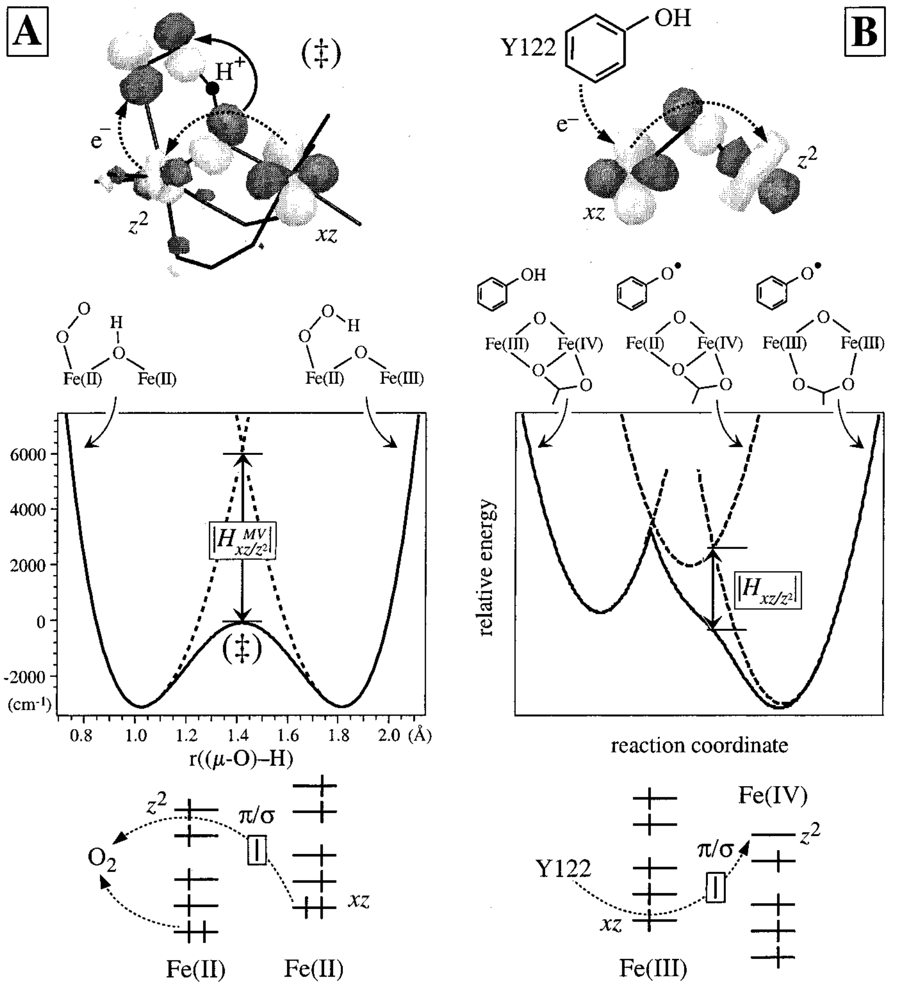

Figure 8. Extension of the results obtained for μ-O,Me$_3$tacn to binuclear non-heme iron proteins. (A) Top: transition state in the PCET reaction of dioxygen binding to deoxyHr (modified from ref 17). Note the favorable orbital arrangement in the mixed Fe−O−Fe π/σ superexchange pathway for ET from the noncoordinated Fe center to O$_2$ binding at the open coordination site of the second iron. Middle: lower sheet of the adiabatic proton PES for the PCET reaction, defined through DFT calculations and modeled by a quartic potential[17] (solid line), and corresponding diabatic potentials (dotted lines).[77] As indicated, the large value of $|H^{MV}_{xz,z^2}| \approx 6000$ cm^{-1} leads to a significant reduction in the Franck−Condon barrier. Bottom: Electronic configurations relevant to the ET process. (B) Top: Schematic illustration of the possible role as an ET pathway of the (putative) mixed π/σ Fe(III)−O−Fe(IV) superexchange pathway in the reaction of R2 intermediate **X** ($\angle$(Fe−O−Fe) $\approx 90°$) with Y122. Middle: relevant PESs in the reaction of **X** with Y122 (solid line: lowest sheet of the adiabatic PES; dotted lines: diabatic potentials). The reaction coordinate is essentially defined by the Y122−O−H proton coordinate (first stage) and the Fe−O−Fe and ligand rearrangements at the diiron site (second stage). Bottom: low energy $\pi(xz)/\sigma(z^2)$ ET pathway from Y122 to Fe(IV) *via* Fe(III).

mixed valence state, the proper value of the electronic coupling matrix element is obtained by using eq 16. This yields $|H^{MV}_{xz,z^2}| \approx 6000$ cm^{-1},[75] indicating that the ET occurs adiabatically.[54,55] While the electronic transmission factor κ for this reaction will be independent of the electronic coupling matrix element (in the adiabatic limit $\kappa = 1$), $|H^{MV}_{xz,z^2}|$ has a significant effect on the nuclear factor of the PCET rate constant because it modulates the proton potential energy surface (PES) in the vicinity of the cusp,[76] as indicated in Figure 8A (middle).[77] This results in a very small Franck−Condon barrier for the PCET process, leading to an extremely large proton tunneling rate constant of $k_{PT} \approx 7 \times 10^{11}$ s^{-1}.[17] It should be noted that the mixed π/σ superexchange pathway plays a further role in that it produces the dominant contribution to the large antiferromagnetic exchange coupling in oxyHr where the singlet ground-state component is stabilized relative to the $S = 5$ component by $30|J| \approx 2310$ cm^{-1} or 6.6 kcal/mol. Notably, this stabilization accounts for ~50% of the thermodynamic driving force for O$_2$ binding to Hr.[18]

The mixed π/σ Fe(xz)−O−Fe(z^2) superexchange pathway might also play an important role in the key reaction steps of O$_2$ activating binuclear non-heme iron enzymes, in particular in ribonucleotide reductase (R2 subunit). The reaction of the reduced diferrous site of R2 with dioxygen leads to the formation of a high-valent Fe(III)/Fe(IV) intermediate termed **X** that

---

[75] Detailed electronic structure studies of the several MV $^1/_2$metHr species have been published (McCormick, J. M.; Reem, R. C.; Solomon, E. I. *J. Am. Chem. Soc.* **1991**, *113*, 9066.). These species are not directly relevant to the O$_2$ binding process, however, because they possess hydroxo bridges at their binuclear sites whereas the MV reaction intermediate has an oxo bridge. Consistent with the decrease in efficiency of the μ-OH superexchange pathway, the values obtained for the electronic coupling matrix elements from analysis of the intervalence transfer spectra of $^1/_2$metHr species, $|H_{\mathrm{Fe(II)/Fe(III)}}| \approx 100-250$ cm^{-1}, is significantly smaller than $|H^{MV}_{xz,z^2}| \approx 6000$ cm^{-1}.

[76] Sutin, N. S. *Prog. Inorg. Chem.* **1983**, *30*, 441.

[77] The adiabatic proton PES for the PCET process shown in Figure 8A (middle) was obtained for a fixed Fe−O$_2$H bond length of 2.75 Å in which case the two minima of the surface connecting the initial and the final states in the reaction are isoenergetic. The proton reaction coordinate was defined by interpolating between the (partially) geometry optimized initial and final state models using DFT calculations. Thus, the proton coordinate correlates between the hydroperoxide-bound, oxo-bridged site and the peroxide-bound, hydroxide-bridged site. See ref 17 for further details.

generates the catalytically essential Tyr122$^\bullet$ free radical.[78] Mössbauer studies on **X** have shown that the more oxidized iron is farther from Tyr122,[79] suggesting that formation of Tyr122$^\bullet$ involves a PCET rather than a hydrogen-atom abstraction by the Fe(III)/Fe(IV) site of **X**.[70,79] This model is consistent with the moderate kinetic isotope effect of $k_H/k_D \approx 2$ for the formation of Tyr122$^\bullet$.[80] Although details of the geometric structure of **X** remain to be elucidated, EPR, ENDOR, and EXAFS data[81,82] are consistent with an Fe(III)/Fe(IV) center possessing a single oxo bridge and one or two additional monoatom bridges provided by carboxylate oxygens (Fe···Fe separation of ~2.5 Å, ∠(Fe−O−Fe) ≈ 90°) (Figure 8B, middle left). In comparison, the structure of the binuclear site of oxidized R2, obtained from **X** in the reaction with Tyr122, is substantially different, consisting of a μ-oxo, μ-1,3 carboxylato bridged Fe(III)$_2$ core[83] (Fe···Fe separation of ~3.3 Å, ∠(Fe−O−Fe) ≈ 120°) (Figure 8B, middle right). Despite the necessity of major nuclear rearrangements at the diiron core upon conversion of **X** into oxidized R2, this process occurs without formation of detectable intermediates. A possible role of the putative mixed π/σ Fe(xz)−O−Fe(z^2) superexchange pathway in this process is illustrated in Figure 8B (middle). In contrast to Hr, the electronic coupling between the substrate and the diiron cluster in R2 is small, giving rise to a substantial Franck−Condon barrier to the ET from Y122 to **X** where the corresponding reaction coordinate is essentially defined by the proton dissociating from Y122 (yielding Tyr122$^\bullet$). This difference is reflected in the rate constants for O_2 binding to deoxyHr, $k_{on} = 7.4 \times 10^6$ M^{-1} s^{-1},[18] and for the reaction of **X** with Y122, $k_{obs} \approx 1$ s^{-1}.[78] While in the diabatic limit (dotted PESs) the subsequent conversion of the virtual Fe(II)/Fe(IV) intermediate into oxidized Fe(III)$_2$ R2 would be associated with a substantial activation barrier (where the reaction coordinate (Figure 8B, middle) is now defined by the Fe−O−Fe and ligand motions (i.e., carboxylate shifts) at the diiron core), the large value of $|H_{xz,z^2}|$ associated with the mixed π/σ superexchange pathway (Figure 8B, top) effectively removes this barrier, leading to a smooth conversion of **X** into the oxidized R2 site. Significantly the mixed π/σ pathway should afford a large electronic coupling matrix element between a low-lying, π-antibonding d orbital on the Fe(III) center and the unoccupied z^2 orbital on Fe(IV) (Figure 8B, bottom), which would permit ET from Tyr122 to Fe(IV) without transient formation of an electronically excited state of the ferric center. Spectroscopic and computational studies on the electronic structures of synthetic oxo-bridged Fe(III)/Fe(IV) complexes are underway to evaluate this model.[84]

In summary, the strong variation of the polarized absorption intensity of μ-O,Me$_3$tacn with temperature provides direct experimental evidence that the mixed π/σ Mn(xz)−O−Mn(z^2) superexchange pathway is the most efficient exchange coupling pathway in bent oxo-bridged Mn(III)$_2$ dimers. The weak ferromagnetic coupling in the ground state of μ-O,Me$_3$tacn arises from a balance between ferromagnetic and antiferromagnetic contributions to J. In the LF excited states this balance is perturbed in favor of antiferromagnetic contributions associated with the mixed π/σ superexchange pathway, leading to a dramatic red-shift of the dominant absorption feature in the visible spectral region with increasing temperature (Figure 2, band *II*). In contrast, the absorption spectrum of OH-bridged Mn(III)$_2$ dimers should be essentially temperature independent due to a large stabilization of the O p orbitals in hydroxide and the consequent weakening of the Mn(III)−O(H) bonding interactions,[26] suggesting that investigation of the temperature dependence of the electronic absorption spectrum of binuclear Mn(III)$_2$ sites should permit discrimination between oxo- and hydroxo-bridged Mn(III)$_2$ core structures. Analysis of ground-state exchange coupling in homovalent dimers in terms of the VBCI model reveals that the contribution to J from a superexchange pathway can be used to estimate the magnitude of the corresponding matrix element for ET, $(H_{AB})^2 = -n(n+1)JU$, which can be scaled to obtain the corresponding value for the one-electron reduced mixed-valence analogue, $H_{AB}^{MV} \cong {}^1/_2 H_{AB}$. When this formalism is applied to μ-O,Me$_3$tacn to estimate the electronic coupling matrix element associated with the mixed π/σ superexchange pathway in bent oxo-bridged dimers, a large value for $|H_{AB}|$ is obtained (~6000 cm^{-1}), indicating that an ET involving this pathway will occur adiabatically. The large coupling matrix element also significantly lowers the Franck−Condon barrier to ET and is key to the high rate constant for the PCET process in the oxygenation reaction of deoxyHr. In addition, it produces a large thermodynamic stabilization of the oxidized site and thus provides about half the driving force for O_2 binding. In ribonucleotide reductase, the mixed π/σ superexchange pathway could serve the role of an efficient ET pathway in the reaction of the Fe(III)/Fe(IV) intermediate **X** with Y122 to generate the Tyr122$^\bullet$ radical required for catalysis.

Acknowledgment. We thank Marshall Hampton for his help with the preparation and preliminary spectroscopic characterization of μ-O,Me$_3$tacn. Financial support by the NSF-Biophysics Program Grant MCB 9816051 is gratefully acknowledged.

Supporting Information Available: Input coordinates for DFT calculations on μ-O,Me$_3$tacn, variable-temperature solid-state mull absorption spectra of the weakly antiferromagnetically coupled dimer [Mn(III)$_2$O(OAc)$_2$(H$_2$O)$_2$(bipy)$_2$](PF$_6$)$_2$·(H$_2$O)$_{1.75}$ ($J = -3.4$ cm^{-1}), many electron wave functions for the $S = 0$ and $S = 4$ components of the dimer ground state, and a schematic energy level diagram illustrating the ferromagnetic and antiferromagnetic contributions from the mixed π/σ superexchange pathway to J (PDF). This material is available free of charge *via* the Internet at http://pubs.acs.org.

JA000264L

---

[78] (a) Ravi, N.; Bollinger, J. M., Jr.; Huynh, B. H.; Edmondson, D. E.; Stubbe, J. *J. Am. Chem. Soc.* **1994**, *116*, 8007. (b) Bollinger, J. M., Jr.; Tong, W. H.; Ravi, N.; Huynh, B. H.; Edmondson, D. E.; Stubbe, J. *J. Am. Chem. Soc.* **1994**, *116*, 8015. (c) Bollinger, J. M., Jr.; Tong, W. H.; Ravi, N.; Huynh, B. H.; Edmondson, D. E.; Stubbe, J. *J. Am. Chem. Soc.* **1994**, *116*, 8024.

[79] Bollinger, J. M., Jr.; Chen, S.; Parkin, S. E.; Mangravite, L. M.; Ley, B. A.; Edmondson, D. E.; Huynh, B. H. *J. Am. Chem. Soc.* **1997**, *119*, 5976.

[80] Private communication with J. Martin Bollinger, Pennsylvania State University, PA.

[81] (a) Willems, J.-P.; Lee, H.-I.; Burdi, D.; Doan, P. E.; Stubbe, J.; Hoffman, B. M. *J. Am. Chem. Soc.* **1997**, *119*, 9816. (b) Burdi, D.; Willems, J.-P.; Riggs-Gelasco, P. J.; Antholine, W. E.; Stubbe, J.; Hoffman, B. M. *J. Am. Chem. Soc.* **1998**, *120*, 12910.

[82] Riggs-Gelasco, P. J.; Shu, L.; Chen, S.; Burdi, D.; Huynh, B. H.; Que, L., Jr.; Stubbe, J. *J. Am. Chem. Soc.* **1998**, *120*, 849.

[83] Nordlund, P.; Eklund, H. *J. Mol. Biol.* **1993**, *232*, 123.

[84] Skulan, A. J.; Hanson, M. A.; Gamelin, D. R.; Que, L., Jr.; Solomon, E. I. Unpublished results.